UC Santa Cruz
2010 International Summer Institute for Modeling in Astrophysics

Title
Spin-down of protostars through gravitational torques

Permalink
https://escholarship.org/uc/item/8618016r

Authors
Lin, Min-Kai
Krumholz, Mark
Kratter, Kaitlin

Publication Date
2010-09-01

Spin down of protostars through gravitational disc torques

Min-Kai Lin,[1,2*] Mark R. Krumholz[1] and Kaitlin M. Kratter[3]

[1] *Department of Astronomy , University of California, Santa Cruz, CA 95064, USA*
[2] *Department of Applied Mathematics and Theoretical Physics, University of Cambridge, Cambridge CB3 0WA, U.K*
[3] *Department of Astronomy and Astrophysics , University of Toronto, Toronto, Ontario M5R 3H4, Canada*

28 August 2010

ABSTRACT

We present three dimensional hydrodynamic simulations of star-disc systems, focusing on the angular momenta evolution of the central object due to gravitational interactions with the disc. It is found that stellar spin is limited to approximately half its break-up speed. We suggest this is due to deformation of the star with increasing spin, which results in larger spin-down torque by the disc. This self-limited spin-up occurs on a short time-scale when the star is gaining mass. On long time-scales, we find simulations where $m = 1$ is the dominant non-axisymmetric mode, there is limited evolution in stellar spin. The displacement of the star from the centre of mass of the system appears to inhibit evolution of the stellar spin angular momentum, in this case the angular momentum exchange between star and disc is primarily in orbital angular momentum of the star. By contrast, simulations where $m = 1$ is non-dominant, we observe a monotonic decrease in stellar spin. Our experiments suggest a necessary condition for long-term spin down be that the system does not develop significant $m = 1$ mode.

1 INTRODUCTION

We consider the collapse of a spherical cloud with initial rotation, leading to the formation of a star-disc system of mass $M_{\rm sys} = M_d + M_*$, where M_d and M_* are the disc and stellar masses respectively. Such systems were recently studied by Kratter et al. (2010), who found disc properties are essentially described by two dimensionless parameters characterising its mass accretion and rotation rates.

Accretion of material onto the disc is described by the parameter ξ:

$$\xi \equiv \frac{G\dot{M}}{c^3}, \tag{1}$$

where $\dot{M}$ is the mass accretion rate and c is the sound-speed. The cloud rotation, responsible for disc formation, is described by the parameter Γ:

$$\Gamma \equiv \frac{\dot{M}}{M_{\rm sys}\Omega_k}, \tag{2}$$

where Ω_k is the Keplerian orbital frequency of material joining the system from the cloud, assumed to occur at cylindrical radius R_k such that $\Omega_k^2 = GM_{\rm sys}/R_k^3$. It can be shown that

$$R_k = \xi^{1/3}\Gamma^{2/3}ct, \tag{3}$$

where $M_{\rm sys} = \dot{M}t$ has been used. Using definitions above, the disc aspect-ratio h at R_k is given by

$$h = \left(\frac{\Gamma}{\xi}\right)^{1/3}. \tag{4}$$

In this work we shall specify h instead of Γ directly. It follows that $R_k = h^2\xi ct$.

Our goal is to study the effect of gravitational torques exerted by the disc on the stellar spin. This paper is organised as follows. In §2 we describe the governing equations, model setup and numerics. Diagnostic measurements are the described in §3. We present simulation results in §4—§6 and conclude with plans for future work in §7.

2 BASIC EQUATIONS AND MODEL

The evolution of an inviscid, non-magnetic and self-gravitating fluid is governed by the hydrodynamic equations:

$$\frac{D\rho}{Dt} = -\rho\nabla \cdot \boldsymbol{v}, \tag{5}$$

$$\frac{D\boldsymbol{v}}{Dt} = -\frac{1}{\rho}\nabla P - \nabla\Phi \tag{6}$$

$$\rho\frac{De}{Dt} = -\rho\boldsymbol{v} \cdot \nabla\Phi - \nabla \cdot (P\boldsymbol{v}) \tag{7}$$

$$\nabla^2\Phi = 4\pi G\rho, \tag{8}$$

where e is the kinetic plus thermal energy density and other symbols have their usual meanings. The pressure is calculated explicitly via a customised equation of state (EOS)

$$P = c^2\rho^{\gamma_1}\left[1 + \left(\frac{\rho}{\rho_*}\right)^{\gamma_2 - \gamma_1}\right], \tag{9}$$

where c is the isothermal sound speed for a gas temperature of 20K and mean molecular weight $\mu = 2.33$. γ_1, γ_2 and ρ_* are fixed parameters so that provided $\gamma_2 > \gamma_1$, when $\rho \ll \rho_*$, $P \propto \rho^{\gamma_1}$ and when $\rho \gg \rho_*$, $P \propto \rho^{\gamma_2}$. We set $\gamma_1 = 1.00001$ and $\gamma_2 = 5/3$ throughout.

This EOS attempts to mimic star formation by halting gravitational collapse. For $\rho \ll \rho_*$, the fluid collapses isothermally. The core central density increases and the collapse is eventually halted by the increased pressure (relative to isothermal EOS). The central object is then effectively a polytrope with polytropic index $n = 3/2$. Because it has finite volume, it may be deformed due to its spin. The non-axisymmetric object may then be spun down due to gravitational torques from the disc.

2.1 Simulation setup

Simulations are initialised with an isothermal sphere of radius r_c, within which the density is

$$\rho = \frac{Ac^2}{4\pi G r^2}, \tag{10}$$

where r is the spherical radius. The dimensionless parameter A relates to the accretion rate ξ, such that $\xi = (2A)^{3/2}/\pi$ for $A \gg 2$. We use tabulated values of A-ξ pairs from Shu (1977). The region $r \leqslant r_* \equiv q r_c$ is designated as the initial star, where q is a dimensionaless parameter. This sets $\rho_* = \rho(r_*)$ and is fixed throughout the simulation. The sphere is initalised with a azimuthal velocity

$$v_\phi = 2Ach \times \begin{cases} R/r_* & R \leqslant r_* \\ 1 & R > r_*, \end{cases} \tag{11}$$

where R is the cylindrical radius. The initial star has solid body rotation. Given the stellar mass M_* and initial radius r_* we require at initialisation that

$$v_\phi(r_*) < \sqrt{\frac{GM_*}{r_*}} \equiv v_{\text{break}}, \tag{12}$$

so the star is below break-up speed at its equitorial plane ($R = r_*$). Equivalently, the requirement is

$$f \equiv \frac{v_\phi(r_*)}{v_{\text{break}}} = 2h\sqrt{A} < 1. \tag{13}$$

The initial energy density e inverted from

$$P = (\gamma - 1)\rho(e - |\boldsymbol{v}|^2/2), \tag{14}$$

where P is given by our equation of state and $\gamma \equiv \frac{\partial \ln P}{\partial \ln \rho}$. The latter calculation of γ is also used in the evolutionary equations.

2.2 Numerics

The hydrodynamic equations are evolved using the Godunov-type ORION code (Truelove et al. 1998; Klein 1999; Fisher 2002) in Cartesian co-ordinates (x, y, z). The computational domain is a cube of length $L = 4r_c$. ORION offers adaptive mesh refinement, a key advantage for the multi-scale flow considered here. We use a base grid of 128^3 with 6 levels of refinement, giving the highest effective resolution of 8192^3. We find this an acceptable compromise between resolving the central object and computation time.

A characteristic length-scale for self-gravitating problems is the Jeans length,

$$\lambda_J = c_s\sqrt{\frac{\pi}{G\rho}}, \tag{15}$$

where $c_s^2 = \gamma P/\rho$ is the density-dependent sound-speed. For

a grid spacing δx, a measure of resolution is $\delta x/\lambda_J$. For our equation of state and parameters, we have:

$$\frac{\lambda_J}{\delta x} = \frac{c}{\delta x}\sqrt{\frac{\pi}{G\rho}} \times \left[1 + \frac{5}{3}\left(\frac{\rho}{\rho_*}\right)^{2/3}\right]^{1/2}. \tag{16}$$

For example, if $\rho/\rho_* \sim 10$ then the linear resolution is a factor of ~ 3 better than isothermal EOS. The increased pressure for high densities (relative to isothermal) increases λ_J because a larger mass is now required for gravitational activity, giving more cells-per-Jeans length for fixed δx.

For refinement, we use the Jeans number N_J to define a maximum resolvable density ρ_J

$$\rho_J \equiv \left(\frac{cN_J}{\delta x}\sqrt{\frac{\pi}{G}}\right)^2, \tag{17}$$

and we refine if $\rho > \rho_J$ at each grid level. The above is the Jeans density for isothermal equation of state. The Jeans density corresponding to our physical set-up, $\rho_{J,\text{real}}$ is, for large ρ/ρ_*,

$$\frac{\rho_{J,\text{real}}}{\rho_J} = \left(\frac{5}{3}\right)^3 \left(\frac{\rho_J}{\rho_*}\right)^2, \tag{18}$$

thus we see that refinement based on the isothermal Jeans density is a conservative approach. The code will refine at a lower density than the real Jeans density, ensuring the central object is resolved. In our higher resolution runs, more aggressive refinement conditions are imposed, refining if $\rho > 0.5\rho_*$ and also refine to the highest level within the theoretical disc radius R_k and one scale-height in z.

It is important to consider the effect of numerical viscosity when studying rotating fluids in a Cartesian grid. Krumholz et al. (2004) found the numerical dissipation of ORION corresponds to an α viscosity of

$$\alpha_N \simeq 78\frac{GM_*}{c_s^2\delta x}\left(\frac{\Delta r}{\delta x}\right)^{-3.85}, \tag{19}$$

where Δr is the distance from the centre of mass (of the star in our case). This numerical viscosity diverges as $\Delta r \to 0$ (Kratter et al. 2010) and could be a source of angular momentum loss for small objects. We tested this by excluding few innermost cells of the central object when computing angular momenta and found little difference to the case when these cells are included. Angular momentum conservation for self-gravitating, inviscid fluids implies the loss of angular momentum in some volume V only depends on the angular momentum flux out of its surface due to advection and gravitational torques. In order to conclude the angular momentum loss of an object is carried by physical fluxes, the numerical viscosity at the surface must not be too large. Hence, when required, Eq. 19 should be evaluated at the stellar surface and compared to α's due to advection and gravity.

3 DIAGNOSTICS

In this section we define diagnostic measures describing our results. The main stellar measurements are summarised in Table 1. We regard fluid with $\rho \geqslant \rho_*$ as stellar material. This is potentially problematic because once stellar material expands (e.g. due to deformation of the star) such that $\rho \leqslant \rho_*$

it is immediately discounted as stellar. However, in simulations we observe little stellar material becomes non-stellar after reaching $\rho \geqslant \rho_*$. As we are primarily concerned with stellar spin, the characteristic stellar radius S_* is defined from its moment of inertia. The boundary where $\rho = \rho_*$ will generally be non-spherical (non-circular in the equitorial plane). The stellar spin angular momentum is defined with position and velocities of fluid elements with respect to $\boldsymbol{x}_*$, $\boldsymbol{v}_*$. The stellar spin frequency follows naturally from $j_{\rm spin} = S_*^2 \Omega_{\rm spin}$.

The evolution of stellar angular momenta shall be related to the rest of the fluid. For simplicity, the exterior fluid is regarded as a two-dimensional disc in cylindrical co-ordinates centred on the star. It is assumed both the normal to the disc plane and stellar spin axis is parallel to the z axis of the inertial frame. Because the star can move, *disc fluid velocities are defined relative to the star*, although we find using relative velocities or velocities in the inertial frame makes no noticeable difference. The disc is described by the surface density Σ and vertically averaged velocities $\boldsymbol{U}$:

$$\Sigma \equiv \int \rho dz, \quad \boldsymbol{U} = \frac{1}{\Sigma} \int \rho (\boldsymbol{v} - \boldsymbol{v}_*) dz, \qquad (20)$$

and we integrate over a slab of constant thickness. Our results are insensitive to the extent of vertical integration.

To analyse various disc modes, the surface density is Fourier transformed in azimuth,

$$a_m \equiv \int \Sigma \exp im\phi d\phi, \qquad (21)$$

where m is the azimuthal wave-number. The pattern speed Ω_p is then $\Omega_p \equiv \dot{\phi}_m/m$ with $\tan \phi_m = -\Im(a_m)/\Re(a_m)$. The integrated amplitude $C_m = \int a_m dr$ is used to examine time evolution of non-axisymmetric modes.

The central theme of this work is star-disc angular momentum transport. We therefore define advective and gravitational angular momentum fluxes

$$F_A = r\Sigma \delta U_\phi \delta U_R, \qquad (22)$$

$$F_G = \int dz \partial_R \Phi \partial_\phi \Phi / 4\pi G \qquad (23)$$

F_A is the angular momentum flux due to Reynolds stress, so $\delta U_\phi = U_\phi - \langle U_\phi \rangle$ where $\langle \cdot \rangle$ is an azimuthal average. F_G is the angular momentum flux associated with self-gravitational torques. These fluxes can be non-dimensionalised into an α viscosity (Kratter et al. 2010), denoted α_R, α_G for Reynolds and gravity respectively. We also calculate the torque exerted by the star on the disc. The stellar potential Φ_* is obtained from $\nabla^2 \Phi_* = 4\pi G \rho_{\rm star}$ where $\rho_{\rm star}$ is the part of the density field with $\rho \geqslant \rho_*$. The torque exerted on the disc per unit area is then $-\Sigma \partial_\phi \Phi_*$.

4 CASE 1

We begin by examining a reference case with physical parameters $\xi = 5.58$ (or $A = 4.0$), $h = 0.1$, $q = 0.005$. We use a Jeans number of $N_J = 0.25$, which is a relatively low resolution with the finest grid cells dedicated to the star. The star is typically resolved by 20 cells in diameter in the $x-y$ plane.

Table 1. Definition of stellar measurements

Name	Symbol	Definition
Mass	M_*	$\int \rho dV$
Position	$\boldsymbol{x}_*$	$\int \boldsymbol{x} \rho dV / M_*$
Velocity	$\boldsymbol{v}_*$	$\int \boldsymbol{v} \rho dV / M_*$
Size	S_*	$\left\{ \int \left[\Delta x^2 + \Delta y^2 \right] \rho dV / M_* \right\}^{1/2}$
Orbital ang. mom.	$j_{\rm orb}$	$\boldsymbol{x}_* \wedge \boldsymbol{v}_* \cdot \hat{\boldsymbol{z}}$
Spin ang. mom.	$j_{\rm spin}$	$\int \rho \Delta \boldsymbol{x} \wedge \Delta \boldsymbol{v} \cdot \hat{\boldsymbol{z}} dV / M_*$
Spin freq.	$\Omega_{\rm spin}$	$j_{\rm spin}/S_*^2$
Break-up freq.	$\Omega_{\rm break}$	$\sqrt{GM_*/S_*^3}$

Volume integrals are taken over $\rho \geqslant \rho_*$. Symbols preceded by 'Δ' are relative to the star, e.g. $\Delta x = x - x_*$. Components of the stellar position and velocity are sometimes expressed in cylindrical polar co-ordinates, so that $\boldsymbol{x}_* = (R_*, \phi_*, z_*)$, for example. The quantity $\left[\Delta x^2 + \Delta y^2 \right]^{1/2}$ represents a fluid element's cylindrical distance from the stellar position.

4.1 Star evolution and relation to disc structure

The evolution of the stellar mass, angular momenta and spin frequency is shown in Fig. 1. The star gains most of its final mass within the first ~ 150kyr. After this, mass gain occurs on a much longer time-scale: between $t = 150$kyr and $t = 400$kyr, M_* grows by 25%. During the initial phase of rapid mass accretion, $\Omega_{\rm spin}$ rises rapidly, but does not exceed $0.55\Omega_{\rm break}$. This initial phase of self-limited spin-up will be examined more closely with a higher resolution run.

After reaching $0.55\Omega_{\rm break}$, $\Omega_{\rm spin}$ drops rapidly to $\sim 0.495\Omega_{\rm break}$ where spin evolution stops abruptly. The evolution of $\Omega_{\rm spin}/\Omega_{\rm break}$ after $t \sim 100$kyr is somewhat erratic with no clear trend of spin up or down, though its variation decreases with time. Compared to initial phases, $\Omega_{\rm spin}/\Omega_{\rm break}$ is effectively constant towards the end of the simulation. The long term non-evolution of $\Omega_{\rm spin}$ is also reflected in $j_{\rm spin}$ in Fig. 1(c). Fig. 1(c) show the evolution of orbital angular momentum is much more active than $j_{\rm spin}$. $j_{\rm orb}$ oscillates between positive and negative values but note that $|j_{\rm orb}|$ and $|j_{\rm spin}|$ are comparable. Notice also the start of the oscillations in $j_{\rm orb}$, near $t \sim 100$kyr, coincides with the abrupt stopping in spin evolution. This suggests that if the star begins to gain significant orbital motion compared to its spin, then its spin evolution may be inhibited.

There are correlations between evolutionary plots above and the disc morphology, shown in Fig. 2. At $t = 43$kyrs (when $\Omega_{\rm spin}/\Omega_{\rm break}$ maximises) the star is highly deformed because it has acquired angular momentum from the disc. It is subsequently spun down by the disc.

Gravitational activity in the disc is apparent at $t = 108$kyr. This is associated with the abrupt stopping in the evolution of $\Omega_{\rm spin}/\Omega_{\rm break}$, but marks the beginning of oscillations in $j_{\rm orb}$ (i.e. $|j_{\rm orb}|$ starts to increase). The density map shows two spiral arms but the arm to the left of the star is more open, whereas the right arm is more tightly wound. Note that the star is no longer as deformed compared to $t = 43$kyr. Because the disc-on-star torque increases in magnitude with non-axisymmetry of the star, at $t = 108$kyr this torque will be relatively smaller than that in $t = 43$kyr, hence the limited evolution in $\Omega_{\rm spin}/\Omega_{\rm break}$ afterwards. If the star is perfectly axisymmetric, large-scale spirals can not alter $j_{\rm spin}$, but may still affect $j_{\rm orb}$.
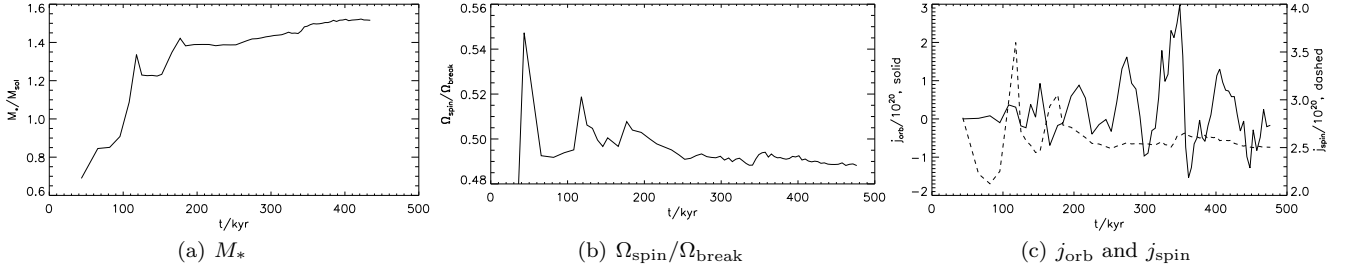
Figure 1. Case 1: stellar mass, spin frequency (scaled by break-up frequency) and angular momenta evolution.

The last two density snapshots in Fig. 2 show decreased gravitational activity in the disc, although an $m = 2$ mode exists close to the star. The $m = 2$ spirals are more prominent at this point than at $t = 43$kyr, but early evolution is associated with large variations in $\Omega_{\rm spin}/\Omega_{\rm break}$ whereas for $t > 250$kyr, $\Omega_{\rm spin}/\Omega_{\rm break}$ is approximately constant. This suggests it is difficult to spin down the star well below 50% break-up speed because at $t > 250$kyr the star is not very deformed. However, there may be additional hindrance from other spiral modes, discussed in the next subsection.

Vertically averaged velocity fields and Toomre Q parameter at $t = 393$kyr is shown in Fig. 3. One-dimensional profiles are also shown. U_R shows strong non-axisymmetry, with velocities up to twice the isothermal sound speed, and can be either sign, resulting in a subsonic azimuthally averaged radial velocity and close to is zero in the disc. Note that $\langle U_R \rangle$ changes sign at $0.045L$. The pattern speed of spiral modes is $\Omega_p \sim 0.3 - 0.5 \times 10^{-11}$, putting co-rotation at $\sim 0.03L$—$0.04L$ from the star and is outside R_k. It is known that self-gravitating discs support modes with co-rotation outside their domain (Papaloizou & Savonije 1991). This is consistent with outwards transport of angular momentum across co-rotation. Material inside co-rotation lose angular momentum and accretes onto the star, while material outside carries that angular momentum outwards. The rotational speed $|U_\phi|$ is typically an order of magnitude larger than $|U_R|$. U_ϕ is consistent with the Q, where lower $|U_\phi|$ regions corresponding to $Q < 1$. The two-dimensional maps show lopsidedness of the various quantities, particularly in U_ϕ. This indicates the presence of a $m = 1$ mode, though this is not visible in the density plots.

4.2   Dominance of $m = 1$

The evolution of stellar properties can be related to non-axisymmetric modes in the disc. Fig. 4 show radial dependence of surface density Fourier amplitudes with $m = 1$—3 (at $t = 393$kyr) and their time evolution. At $t = 393$kyr, Eq. 3 implies a disc radius of $R_k/L \simeq 0.023$, (or $0.46l$, where $l = 0.05L$), consistent with the surface density map in Fig. 2.

Fig. 4(a) show that $m = 2$ is dominant close to the star, consistent with 2D maps. However, $m = 1$ dominates in the remainder of the disc, and also well beyond R_k. Although $m = 2$ dominates again in the outermost region (but its amplitude is still smaller than the interior $m = 1$), it is ineffective in spinning the star down because far away, the
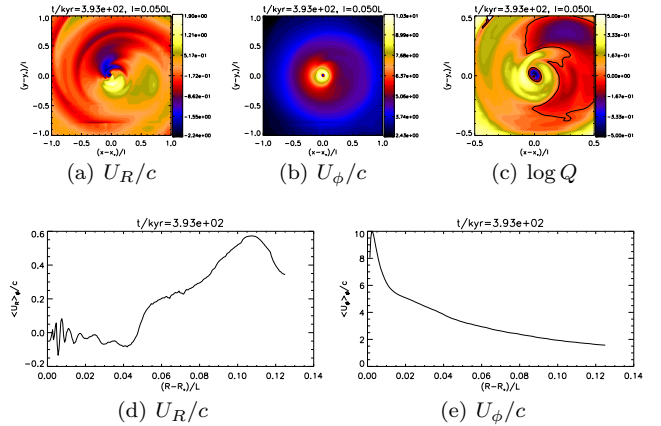

Figure 3. Case 2: vertical averaged velocities relative to the star and the Toomre Q distribution. Contour lines in the Toomre Q plot indicate the $Q = 1$ curve.

star resembles a point mass, hence the far field $m = 2$ has little influence on $\Omega_{\rm spin}$.

Fig. 4(b) show the time evolution of radially integrated mode amplitudes. Dominance of $m = 2$ occurs early on when the star gains most of its mass. During this phase, the star spins up, deforms, then spin down (see §5). However, $m = 1$ over-takes around $t \sim 100$kyr, which is also when spin-down from $\max(\Omega_{\rm spin}/\Omega_{\rm break})$ stops and $|j_{\rm orb}|$ begins to increase. At $t > 100$kyr, the $m = 2, 3$ modes decays, while the $m = 1$ mode remains approximately constant in strength; and $\Omega_{\rm spin}/\Omega_{\rm break}$, $j_{\rm spin}$ evolves very little (Fig. 1).

There is clear correlation between dominance of $m = 1$ and non-evolution of $\Omega_{\rm spin}$. One effect of the $m = 1$ mode is to displace the central star away from the centre of mass of the box (Adams et al. 1989; Heemskerk et al. 1992). Indeed, the star does exhibit a somewhat complex orbital motion (Fig. 5). Its displacement over the simulation is a few per cent of of the box size L, comparable to the theoretical disc size of $0.02L$ and its characteristic size S_*. When treated as a point mass the star only has angular momentum in the form of orbital motion. In our case the star has finite size, but the $m = 1$ still preferentially modifies $j_{\rm orb}$ instead of $j_{\rm spin}$.

Another difference between our simulations and early theoretical work is that, in the latter the orbital frequency of the star about the centre of mass of the domain is comparable to the mode pattern speed. In our case, the orbital frequency is less than Ω_p. This suggest that the $m = 1$ mode is not primarily driven by the star.
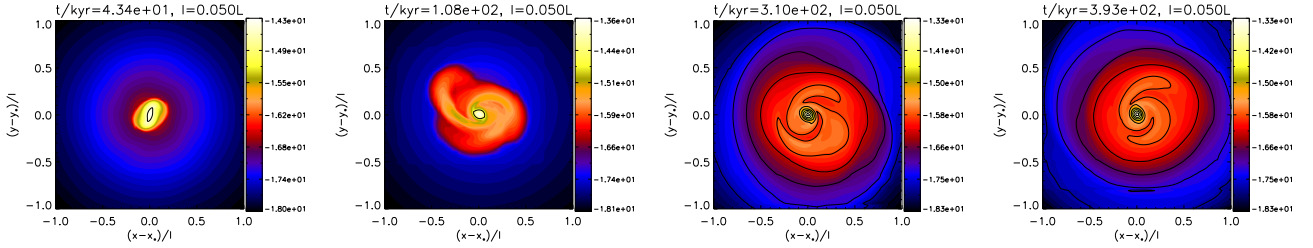
Figure 2. Case 1: evolution of $\log\rho$. In the first two snapshots, contour lines indicate region within which $\rho > \rho_*$. In the other plots, additional contour lines are shown to highlight the spiral structures. These plots are to be compared to evolutionary plots above.
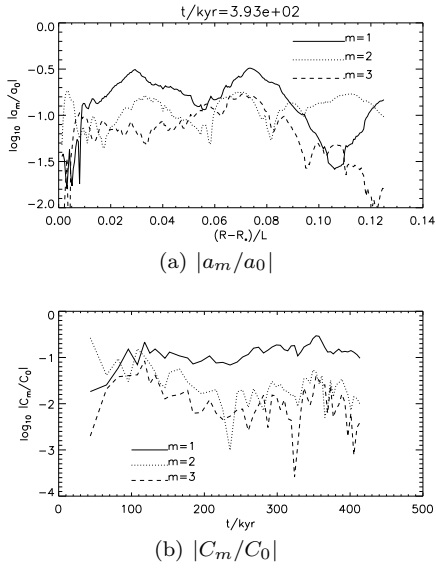
Figure 4. Case 1: mode amplitudes as a function of cylindrical distance from the star and time-evolution of the integrated mode amplitudes. The star has size $S_*/L \simeq 1.75 \times 10^{-3}$.
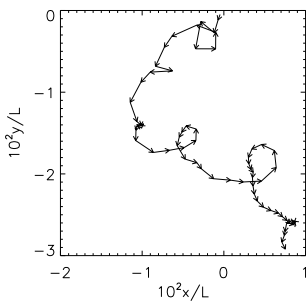
Figure 5. Case 1: star motion in an inertial frame.

5 CASE 1: SELF-LIMITED SPIN UP

We re-examine early evolution $30\mathrm{kyr} \leqslant t \leqslant 70\mathrm{kyr}$ of Case 1 with improved resolution (see §2.2). Fig. 6 show snapshots of the density field, spin and angular momenta evolution. As seen in the lower resolution run, early on there is rapid increase in j_{spin} and $\Omega_{\mathrm{spin}}/\Omega_{\mathrm{break}}$ until $t = 40\mathrm{kyr}$. Until this time the star is highly deformed but no spiral arms are present. During $40\mathrm{kyr} < t < 50\mathrm{kyr}$, j_{spin} remains approximately constant and spiral arms develop in the disc ($t = 47\mathrm{kyr}$). From $t = 52\mathrm{kyr}$ $t = 67\mathrm{kyr}$ spiral arms are al-

ways present and j_{spin} is decreasing. $\Omega_{\mathrm{spin}}/\Omega_{\mathrm{break}}$ also maximise around $t = 40\mathrm{kyr}$, it then oscillations with decreasing amplitude and by $t = 70\mathrm{kyr}$ it is just below 50% of break-up. Notice that $|j_{\mathrm{orb}}|/|j_{\mathrm{spin}}| \sim 10^{-3}$ and the star is essentially fixed in the inertial frame.

As the star accretes material and therefore angular momentum, its spin increases (provided S_* does not decrease significantly, which is expected because the EOS prevents further collapse). However, as it spins up, it becomes deformed by centrifugal forces. The object has high $m = 2$ symmetry, analogous to a bar, which exerts a positive gravitational torque on the surrounding material because it spins faster than the disc. The star must then lose spin angular momentum. Thus the initial spin-up is limited by the fact that spin-down torques from the disc increases as the star spins up and deform into a bar.

The torque exerted by the star on the disc is shown in Fig. 7(b), for the snapshot at $t = 60\mathrm{kyr}$ during spin-down. The star exerts a positive torque on the disc, and is largest just outside its surface. Spin angular momentum lost by the star is mostly deposited in this material. Fig. 7(c) show angular momentum fluxes due to Reynolds stresses and gravity torques. At the stellar interface, these sum to $\alpha \sim 0.3$ with positive contribution from gravity ($\alpha_G \sim 0.7$) and negative contribution from Reynolds stresses. Replacing the Reynolds stress by the total advection $r\Sigma U_r U_\phi$ results in a total $\alpha \sim 0.7$ at the same radius. The large-scale advection is nearly zero at the interface, indicating no flow of material across its surface (hydrostatic object). The numerical viscosity is $\alpha_N \sim 0.03$ at the interface, so the angular momentum carried away from the star is largely due to gravitational torques.

6 CASE 2

We now consider a case where $m = 1$ is not dominant over the simulation time-scale, using physical parameters $\xi = 2.74$ (or $A = 2.8$), $h = 0.05$ and $q = 0.01$. Displacement of the star by the $m = 1$ mode require massive discs ($M_d \geqslant M_*$, Heemskerk et al. (1992)), so a lower ξ is used, corresponding to a smaller core mass compared to Case 1. A smaller h indicates smaller angular momentum in the core. q is increased, corresponding to a larger initial star, which should be more vulnerable to deformation. Overall, this set-up produces a quieter evolution. We use $N_J = 0.125$ for this run.

(e) Spin frequency   (f) Angular momenta
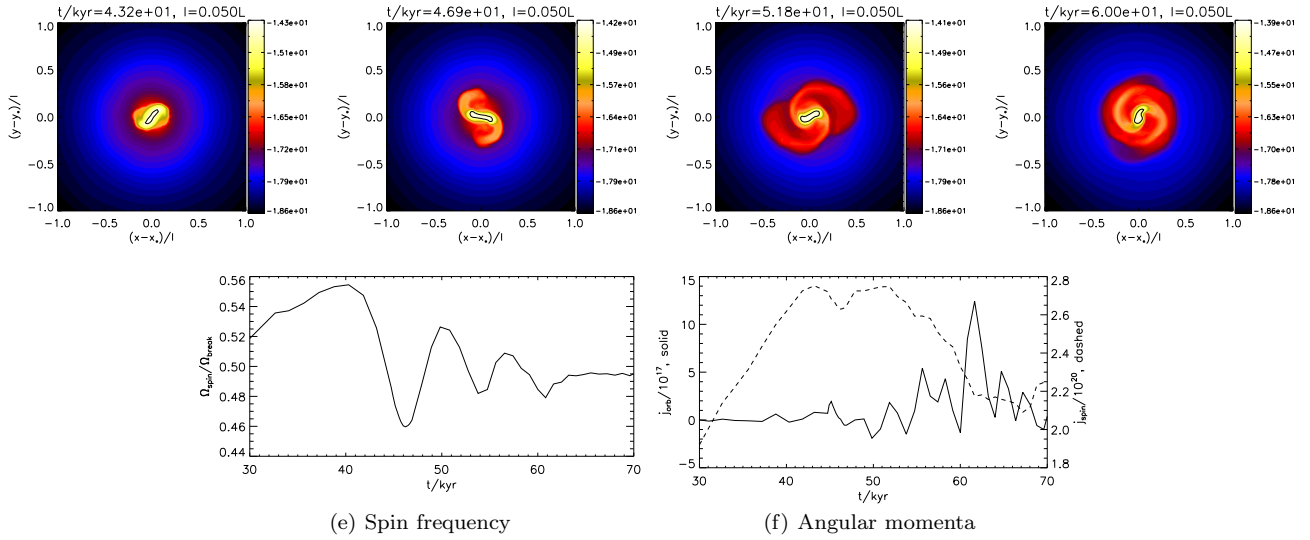
Figure 6. Case 1 high resolution: density field (top panel), spin frequency relative to break-up and angular momenta (bottom panel). The time interval corresponds to early evolution where the initial spin-up is self-limited by deformation of the star (outlined by thick lines in the top figures).

(a) Density field   (b) Star-disc torque   (c) Angular momentum flux
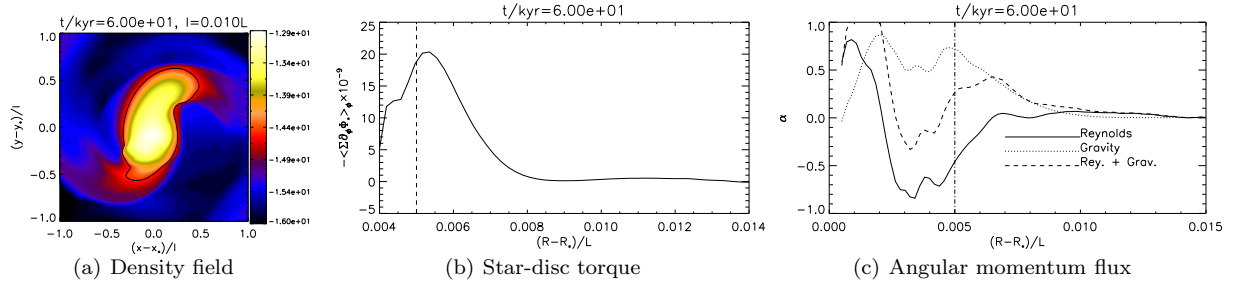
Figure 7. Case 1 high resolution: density field during initial spin down phase (left), the corresponding star-on-disc torque (middle) and angular momentum fluxes (right). Vertical lines in the last two plots indicate the semi-major axis of the deformed star when regarded as an ellipse.

6.1   Star evolution and relation to spiral modes

Fig. 8 show the evolution of stellar measurements in conjunction with results from Fourier analysis of the surface density. Despite changing more than one parameter from Case 1, early evolution is indifferent. The star acquires most of its final mass by $t = 400$kyr, M_* then remain approximately constant. During mass growth, $\Omega_{\rm spin}/\Omega_{\rm break}$ also increase rapidly but again *does not exceed* $\sim 50\%$ *break-up*. However, there is now a clear monotonic decrease in rotation after $\Omega_{\rm spin}$ maximises, whereas Case 1 experienced multiple episodes of brief spin-up (Fig. 1). For Case 2, the final $\Omega_{\rm spin}/\Omega_{\rm break}$ is about 92% of $\max(\Omega_{\rm spin}/\Omega_{\rm break})$ and in Case 1 it is $\sim 90\%$, i.e. more overall spin-down in Case 1. However, in Case 1 most of the spin-down was attributed to the phase just after $\max(\Omega_{\rm spin}/\Omega_{\rm break})$, whereas in Case 2 there is continued spin-down on the simulation time-scale, suggesting Case 2 could spin down more if continued. No obvious future trend could be speculated for Case 1. The angular momenta plot show that $|j_{\rm orb}|$ is an order of magnitude smaller than $|j_{\rm spin}|$, and is correlated to the presence of long term spin down, unlike Case 1.

The Fourier amplitudes also differ to Case 1. Fig. 8(d)

show the time evolution of the $m = 1$—3 modes. This physical setup allows $m = 2$ to become dominant. Fig. 8(e) show the radial dependence of Fourier modes at the end of the simulation and $m = 1$ no longer dominates the system throughout. The extent of $m = 2$ is also larger than Case 1, corresponding to the non-axisymmetric (and larger) star. This shows that a star-disc system with dominated by $m = 2$ non-axisymmetry is more prone to spin down.

Case 2 compliments Case 1, in that we have suppressed $m = 1$, thereby allowing spin-down torques to operate effectively on an object that has small orbital motion. Spin down is easier in this case because the disc (which provides the torque) need not be moving with stellar motion. Spin-down torques can not act on the star for an extended period of time if it were moving around.

6.2   Star-disc torques

We need to idenfity the origin of the torque responsible for spin angular momentum loss. We consider the density field at $t = 486$kyr shown in Fig. 8(f), which marks the start of long term spin down. It clearly shows two spirals associated with the star. In Fig. 9 show the star-on-disc torque per

(a) M_*

(b) Stellar rotation

(c) Specific angular momenta

(d) $|C_m/C_0|$

(e) $|a_m/a_0|$

(f) ρ
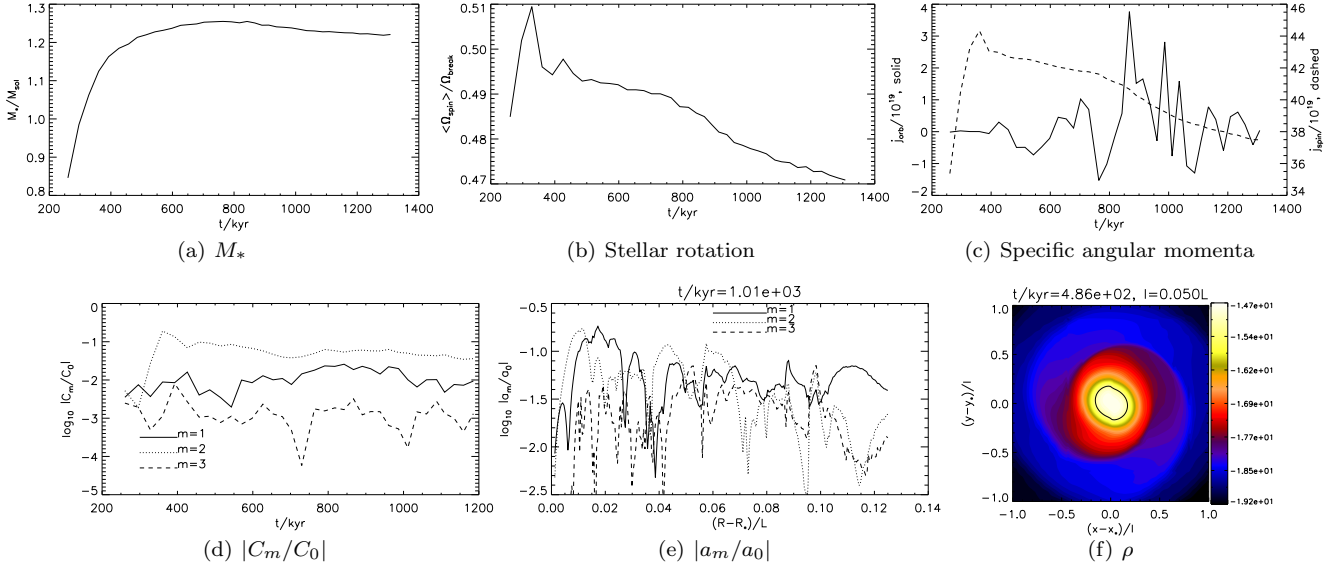
Figure 8. Case 2: stellar mass, spin frequency and angular momenta evolution (top panel); evolution of disc mode amplitudes and their radial dependence at the end of the simulation (bottom panel). The last plot is the density at the beginning of long term spin down, and the stellar interface is indicated by the solid line.

unit area at $t = 486$kyr. The star exerts a positive torque on material just outside its surface, itself losing spin angular momentum. The torque density is not much smaller than Case 1 high resolution (Fig. 7(b)). Note the lack of 'spikes' in this plot, which one may expect if there are resonance effects between tides on the star (from deformation) and disc modes. Dominant spin-down torques occur close to the stellar interface.

In Fig. 10 we compare angular momentum flux carried by Reynolds stresses and gravitational torques. There is a positive gravity flux throughout the disc, but its amplitude is small ($\alpha_G = O(10^{-2})$) compared to values expected for gravito-turbulence ($\alpha_G \sim 0.1$—1). Positive gravity flux at the stellar interface is consistent with the star exerting a positive torque on the disc. The figure show at stellar interface, which is only approximate because the star is not spherical , gravity flux is slightly larger than the (negative) Reynolds stress. The total viscosity is $\alpha \sim 2.5 \times 10^{-3}$.

At the stellar interface indicated in Fig. 10 the numerical viscosity is $\alpha_N \sim 0.06$. Hence, loss of spin angular momentum may largely be attributed to numerical viscosity. Nevertheless, there *is* a positive gravity flux at the stellar interface due to a negative disc torque acting on the star. If we lower the numerical viscosity by increasing resolution and/or increase the core mass to increase gravitational torques, then it is conceivable at some point gravity flux out of the star dominates over numerical dissipation. In that case, we would conclude long-term spin down is due to gravitational torques.

Although spin-down here is attributed to numerics, when compared to Case 1 this run demonstrates that, for spin-down torques to be effective, it is desirable not to have significant hindrance from $m = 1$ moving the star.
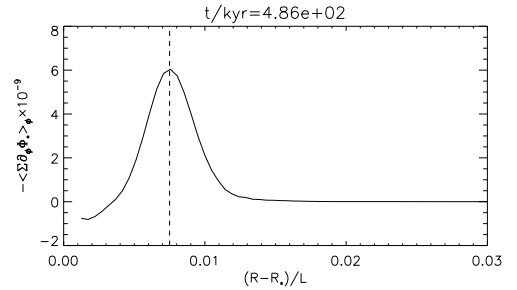
Figure 9. Case 2: azimuthally averaged star-on-disc torque. The horizontal axis is the cylindrical distance from the star and the vertical dashed line indicates the stellar interface (see Fig. 8(f)).
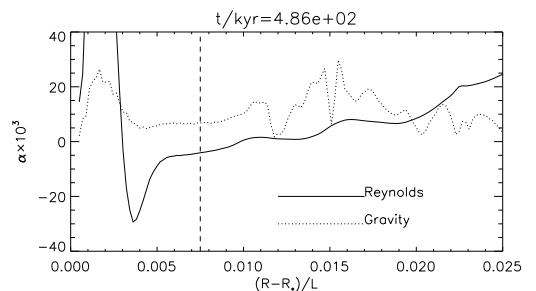
Figure 10. Case 2: angular momentum fluxes non-dimensionalised into α viscosities associated with Reynolds stresses and gravitational torques. The vertical dashed line is where $\rho \simeq \rho_*$, obtained by inspection from Fig. 8(f).

7 CONCLUSIONS AND FUTURE WORK

We have performed three dimensional hydrodynamic simulations star-disc systems self-consistently formed by cloud collapse. Our goal was to assess whether or not gravitational torques can be responsible in spinning down the central star.

The initial spin-up of the star is limited to $\sim 50\%$ of break-up speed because increasing spin also increases the star's deformation into a bar-like object, on which the disc exerts a negative torque.

While the present low resolution simulations do not show strong evidence for gravitational spin-down on long time-scales, we do find a necessary requirement for spin evolution is that $m = 1$ be non-dominant. Otherwise, the displacement of the star from the centre of mass (of the box) results in significant and complex orbital motion, which inhibits spin evolution. In order to explicitly demonstrate gravitational torque spin-down in the later evolutionary stages, higher resolution simulations are required to resolve the star-disc interface, since this is where most of the torque is exerted on the star.

REFERENCES

Adams F. C., Ruden S. P., Shu F. H., 1989, ApJ, 347, 959
Fisher R. T., 2002, PhD thesis, UNIVERSITY OF CALIFORNIA, BERKELEY
Heemskerk M. H. M., Papaloizou J. C., Savonije G. J., 1992, A&A, 260, 161
Klein R. I., 1999, Journal of Computational and Applied Mathematics, 109, 123
Kratter K. M., Matzner C. D., Krumholz M. R., Klein R. I., 2010, ApJ, 708, 1585
Krumholz M. R., McKee C. F., Klein R. I., 2004, ApJ, 611, 399
Papaloizou J. C., Savonije G. J., 1991, MNRAS, 248, 353
Shu F. H., 1977, ApJ, 214, 488
Truelove J. K., Klein R. I., McKee C. F., Holliman II J. H., Howell L. H., Greenough J. A., Woods D. T., 1998, ApJ, 495, 821